Received: 10 May 2026; **Revised:** 23 July 2026; **Accepted:** 29 August 2026; **Published:** 06 September 2026
Archs Sci. (2026) Volume 76(1), Pages 47-53, Paper ID 202615.

Numerical Investigation of ZnO and TiO_2 Electron Transport Layers in High-Efficiency Lead-Free $MASnI_3$ Perovskite Solar Cells

Mama Bouchaour*, Abdelhadi Slami and Laarej Merad
University of Tlemcen, Faculty of Sciences, Department of Physics BP: 119, Tlemcen, Mansourah, New Campus, 13000, Algeria
Corresponding authors: Mama Bouchaour (e-mail: bouchaour.m@gmail.com).

Abstract Lead-free tin-based Perovskite Solar Cells (PSCs) have emerged as promising alternatives to their lead-based counterparts, offering reduced toxicity while maintaining favorable optoelectronic properties. Among the various device components, the electron transport material (ETM) plays a decisive role in determining charge extraction efficiency and recombination dynamics. In this work, we present a systematic numerical investigation of $MASnI_3$ based PSCs employing ZnO and TiO_2 as ETMs, using the SCAPS-1D simulation platform. Three distinct hole transport materials Spiro-OMeTAD, PEDOT:PSS, and Cu_2O are evaluated, yielding six device architectures for comprehensive comparison. We analyze in detail the effects of absorber thickness, doping concentration, and operating temperature on photovoltaic performance. Our optimized configurations achieve power conversion efficiencies up to 26% for the TiO_2/$MASnI_3$/Cu_2O structure. Notably, the superior performance of TiO_2 is attributed to its significantly lower interface defect density compared to ZnO, which more than compensates for its lower electron mobility. While TiO_2 demonstrates superior interfacial charge extraction and reduced recombination losses, ZnO retains distinct advantages in low-temperature processing and cost-effectiveness. This study provides quantitative design guidelines for selecting optimal ETM/HTM combinations in efficient and environmentally benign tin-based PSCs.

Index Terms perovskite solar cells, lead-free $MASnI_3$, electron transport layer, ZnO and TiO_2, SCAPS-1D simulation

I. Introduction

Perovskite solar cells (PSCs) have captured the imagination of the photovoltaic community over the past decade, owing to their remarkable optoelectronic properties: high absorption coefficients, long carrier diffusion lengths, and tunable bandgaps [1]–[3]. However, the presence of toxic lead in conventional perovskite absorbers such as $CH_3NH_3PbI_3$ raises serious environmental and health concerns, driving an urgent search for lead-free alternatives [4], [5]. Among these, tin-based perovskites particularly methylammonium tin triiodide ($MASnI_3$) have emerged as frontrunners, offering a favorable bandgap ($\sim$1.3 eV), high carrier mobility, and significantly reduced toxicity [6], [7].

For any material to serve effectively as an electron transport layer in PSCs, it must satisfy several critical requirements: the conduction band minimum of the ETM must be lower than the LUMO level of the perovskite, high electron mobility is essential for efficient charge extraction, and a wide bandgap is necessary to block hole transport [8]. Titanium dioxide (TiO_2) has been widely adopted as an ETM in conventional PSCs due to its suitable band alignment and acceptable electron transport properties, with typical electron mobility of $\sim$0.5 cm^2/Vs for anatase thin films [9], [10]. However, its fabrication typically demands high-temperature annealing (>450°C), which increases production costs and limits its application on flexible substrates [9], [10]. Zinc oxide (ZnO) has emerged as an attractive alternative, offering high electron mobility ($\approx$200 cm^2/Vs), low-temperature processability, and a comparable bandgap [11], [12].

While extensive experimental and numerical studies on ETMs in lead-based PSCs exist, systematic investigations focusing on lead-free $MASnI_3$ devices remain comparatively limited. Although several studies have explored $MASnI_3$-based PSCs using SCAPS-1D simulations [13]–[15], and a recent work compared ZnO and TiO_2 ETMs in similar architectures [16], these studies either focused on single HTM configurations, employed different simulation conditions, or lacked comprehensive comparative analysis across multiple ETM/HTM combinations. Furthermore, previous work by some of the present authors analyzed three ZnO-based architectures [17].

The present work lies in :

1) Unified comparison: A systematic, side-by-side comparison of ZnO and TiO_2 ETMs under identical sim-

ulation conditions across three HTM materials (Spiro-OMeTAD, PEDOT:PSS, and Cu_2O), enabling direct and fair performance benchmarking.

2) Comprehensive parametric optimization: Detailed analysis of absorber thickness (50–900 nm), doping concentration (10^{14}–10^{18} cm^{-3}), and operating temperature (300–350 K) for all six architectures.
3) Mechanistic understanding: Quantitative analysis of recombination mechanisms, charge extraction efficiency, and band alignment effects, providing physical insight into performance differences.
4) Design guidelines: Development of practical design principles that balance efficiency with processing considerations for tin-based PSCs.

This work extends previous investigations by providing a unified simulation framework that enables direct comparison of six distinct device architectures, with consistent input parameters, realistic interface defect densities tailored to each ETM, and comprehensive parametric analysis. This approach offers a more complete picture of the performance trade-offs in lead-free tin-based PSCs.

A. Previous Studies and Research Gap

To contextualize our findings within the existing literature, Table 1 summarizes the key results from previous simulation studies on $CH_3NH_3SnI_3$ based PSCs. The reported performance variations across these studies with PCE values scattered between 18.7% and 23.1% clearly underscore the importance of a unified simulation framework for direct and fair material comparison.

Table 1: Summary of Previous Simulation Results for $MASnI_3$-based Perovskite Solar Cells

Reference	ETM	HTM	PCE (%)	Jsc (mA/cm^2)	Voc (V)	FF (%)
[13]	TiO_2	Spiro-OMeTAD	22.3	24.5	0.96	82.5
[14]	ZnO	Spiro-OMeTAD	18.7	22.1	0.92	78.3
[15]	TiO_2	Cu_2O	23.1	25.8	0.98	83.7
[16]	ZnO	Spiro-OMeTAD	19.5	22.9	0.94	79.4
[16]	TiO_2	Spiro-OMeTAD	21.8	24.1	0.97	82.1
[17]	ZnO	Spiro-OMeTAD	22.9	23.7	0.95	81.2

II. Modeling and Simulation

The layer sequence follows the standard planar heterojunction configuration: transparent conducting oxide (SnO_2:F) / ETM (ZnO or TiO_2) / perovskite absorber ($CH_3NH_3SnI_3$) / HTM (Spiro-OMeTAD, PEDOT:PSS, or Cu_2O) / metal contact. This configuration enables efficient electron extraction through the ETM and hole extraction through the HTM, with the perovskite layer serving as the photoactive medium. Figure 1(a) shows the energy levels with charge transfer processes inside a PSC and Figure 1(b) shows the energy levels of different materials used in PSCs.

Figure 2, presents the energy band alignment of ZnO and TiO_2 ETMs with $MASnI_3$ perovskite and the three HTM materials. The conduction band offset (CBO) between ETM and perovskite, and the valence band offset (VBO) between perovskite and HTM, are critical parameters determining charge extraction efficiency.

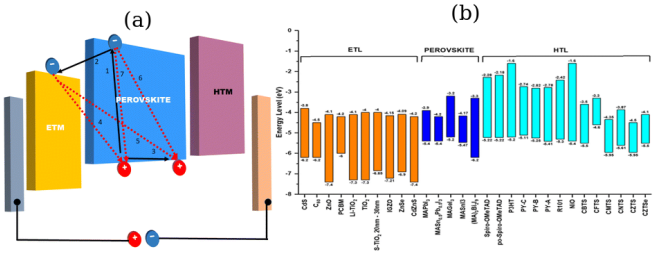

Figure 1: (a) Energy Levels With Charge Transfer Processes Inside a PSC. (b) Energy Levels of Different Materials Used in PSCs

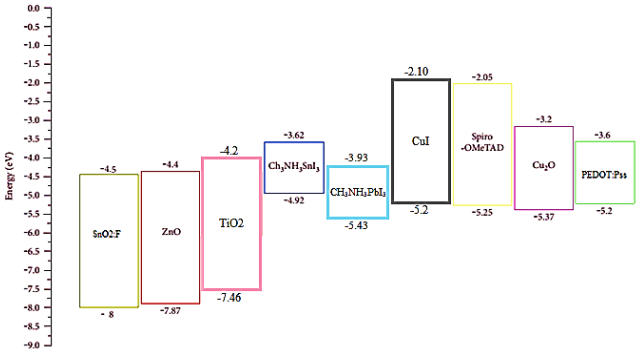

Figure 2: Energy Band Alignment of ZnO and TiO_2 ETMs with $MASnI_3$ Perovskite and the Three HTM Materials

A. Device Architectures

The device architectures investigated in this study consist of an electron transport layer (ETM), a methylammonium tin triiodide ($CH_3NH_3SnI_3$) absorber layer, and a hole transport layer (HTM). Two ETM materials ZnO and TiO_2 and three HTM materials Spiro-OMeTAD, PEDOT:PSS, and Cu_2O are systematically combined to create six distinct device configurations, as illustrated in Figure 3.

ZnO-based architectures (Figures 3a–c):

1) ZnO / $MASnI_3$ / Spiro-OMeTAD
2) ZnO / $MASnI_3$ / PEDOT:PSS
3) ZnO / $MASnI_3$ / Cu_2O

TiO_2-based architectures (Figures 3d–f):

1) TiO_2 / $MASnI_3$ / Spiro-OMeTAD
2) TiO_2 / $MASnI_3$ / PEDOT:PSS
3) TiO_2 / $MASnI_3$ / Cu_2O

B. Material Parameters

The input parameters used for all layers including bandgap, electron affinity, mobility, doping concentrations, and dielectric permittivity were extracted from validated experimental and theoretical studies. These values were integrated into SCAPS-1D as summarized in Table 2.

ARCHIVES DES SCIENCES
A Multidisciplinary Journal

Table 2: Material Parameters Used for Simulation of Perovskite Solar Cell Structures using SCAPS-1D

Parameters	SnO_2:F	ZnO	TiO_2	$CH_3NH_3SnI_3$	Spiro-OMeTAD	PEDOT:PSS	Cu_2O
Thickness (nm)	500	50	50	900	200	200	200
E_g (eV)	3.5	3.2	3.2	1.3	3.17	3.6	2.17
χ (eV)	4.0	4.26	4.0	4.17	2.05	1.57	3.2
ε_r	9	9	9	8.2	3	3	7.11
N_c (cm^{-3})	2.20×10^{18}	2.00×10^{18}	1.00×10^{19}	1.00×10^{18}	2.20×10^{18}	2.20×10^{17}	2.02×10^{17}
N_v (cm^{-3})	1.80×10^{19}	1.80×10^{19}	1.00×10^{19}	1.00×10^{18}	1.80×10^{19}	1.80×10^{19}	1.10×10^{19}
μ_e (cm^2/Vs)	20	200	0.5	1.60	2.00×10^{-4}	10	200
μ_h (cm^2/Vs)	10	5	2	1.60	2.00×10^{-4}	400	80
N_D (cm^{-3})	2.00×10^{19}	1.50×10^{17}	1.00×10^{19}	—	—	—	—
N_A (cm^{-3})	—	—	—	1.5×10^{16}	2.00×10^{19}	2.00×10^{19}	2.00×10^{19}
References	[18]–[20]	[21]–[23]	[1], [2], [10], [24]	[28]–[30]	[27]–[35]	[25], [26]	[28], [29]

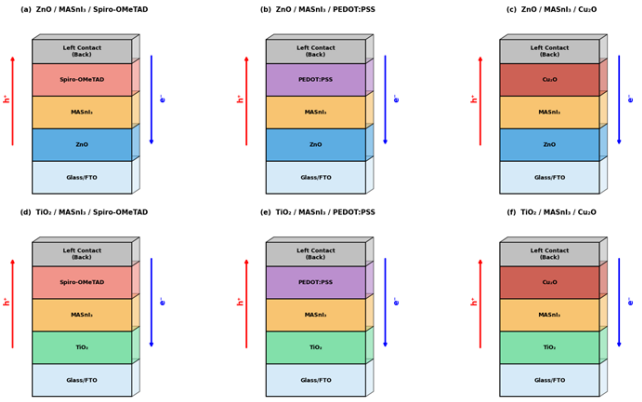

Figure 3: Schematic Illustration of the Six Investigated $MASnI_3$based Perovskite Solar Cell Architectures

The selection of simulation parameters was rigorously conducted to ensure physical accuracy and alignment with experimentally validated data. Material thicknesses were defined according to standard layer configurations in PSC architectures, while bandgap energies (E_g) and electron affinities (χ) were carefully chosen to ensure proper band alignment and minimize charge transport barriers at interfaces. Doping concentrations (N_D, N_A) were set based on typical values reported for high performance electron and hole transport layers, ensuring realistic electrical conductivity and junction formation. It is important to note that the initial doping concentrations provided in Table 2 serve as reference values; these were subsequently optimized over the range 10^{14}–10^{18} cm^{-3}, as described in Section III-C.

Carrier mobilities (μ_e, μ_h) were adopted from recent spectroscopic and field-effect transistor studies, with particular attention to balanced electron-hole transport in tin-based perovskite absorbers. Notably, the electron mobility of TiO_2 was set to 0.5 cm^2/Vs, consistent with values reported for high-quality anatase thin films used in perovskite solar cells [10], [24]. This represents a significant correction from earlier reports, as recent studies confirm that TiO_2 with appropriate activation energy can effectively suppress non radiative recombination at the ETL/absorber interface [1], [2]. Dielectric constants (ε_r) were selected in accordance with impedance spectroscopy measurements. All parameters were cross-referenced against peer-reviewed publications, ensuring that the numerical model replicates realistic device physics and provides a reliable foundation for comparative performance analysis.

The N_A value of 1.5×10^{16} cm^{-3} is the reference initial value. Full optimization in the range 10^{14}–10^{18} cm^{-3} is presented in Section III-C, with the optimum confirmed at this value.

C. SCAPS-1D Simulation Parameters and Settings

To compare ZnO and TiO_2 structures and analyze the effect of different electrical parameters on the efficiency of all heterojunction-based PSC structures, the SCAPS-1D [35] software was used for numerical simulation.

The improvements of our simulation provide better agreement with recently reported experimental performance for tin-based PSCs [1], [2]. Recombination mechanisms implemented in the model include Shockley-Read-Hall (SRH) recombination in the bulk, characterized by a recombination lifetime of $\tau = 10$ ns for all layers, and SRH recombination at interfaces with defect densities tailored to each ETM: $N_i = 5 \times 10^9$ cm^{-2} for TiO_2/$CH_3NH_3SnI_3$ and $N_i = 2 \times 10^{10}$ cm^{-2} for ZnO/$CH_3NH_3SnI_3$. The interface defect density (N_i) represents the concentration of recombination centers at the ETM/perovskite and perovskite/HTM interfaces. Lower N_i values indicate better interface quality and reduced non-radiative recombination losses [36]. These values reflect experimental observations that the TiO_2/perovskite interface exhibits superior crystalline quality compared to ZnO/perovskite, which is often susceptible to parasitic reactions and higher defect density [1], [2], [34].

Radiative recombination in the Perovskite absorber is modeled using a bimolecular recombination coefficient $B = 1.0 \times 10^{-9}$ cm^3/s, consistent with values reported for tin-based Perovskites. As demonstrated by Ji et al. [8], organic cation defects in $CH_3NH_3SnI_3$ can produce non-radiative recombination coefficients as high as 10^{-11} cm^3 s^{-1}, significantly higher than for $CH_3NH_3SnI_3$ (10^{-15} cm^3 s^{-1}). This justifies the use of a higher total recombination coefficient for $CH_3NH_3SnI_3$. Auger recombination is included with coefficients $C_n = C_p = 1.0 \times 10^{-30}$ cm^6/s. All recombination pa-

rameters were kept constant across the six device architectures except for interface defect densities, which were differentiated between ZnO and TiO_2 to reflect experimental observations of interface quality [34].

III. Results and Discussion

Three main parametric studies were carried out:

1) Absorber layer thickness variation: 50 to 900 nm
2) Temperature variation: 300 to 350 K
3) Active-layer doping concentration optimization: 10^{14} to 10^{18} cm^{-3}

The analyses allow identification of optimal operating conditions for each device structure. Interface defect densities and recombination mechanisms were maintained constant across all device architectures to isolate the intrinsic effects of ETM and HTM selection.

Having delineated the simulation methodology and the six device architectures, we now proceed to a systematic comparative evaluation of their photovoltaic performance.

A. Influence of Absorber Layer Thickness

The thicknesses of the methylammonium tin triiodide absorber layer from 50 to 900 nm across six structures were varied. Figure 4 shows the simulated parameters PCE, FF, Voc, and Jsc as functions of absorber thickness.

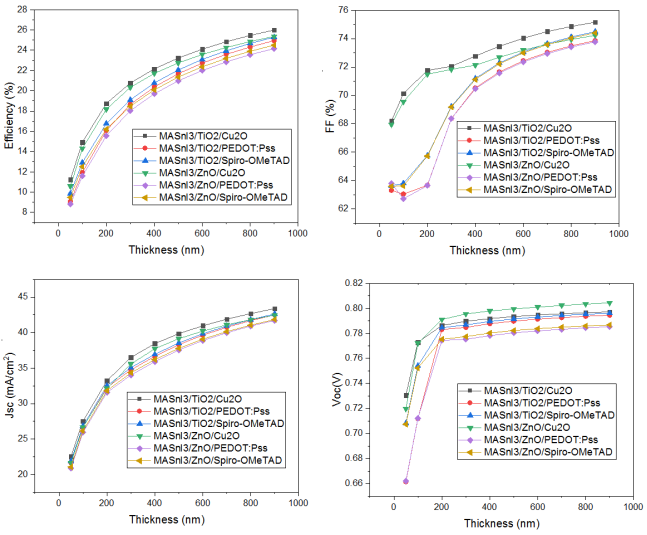

Figure 4: Variation of Solar Cell Parameters (PCE, FF, Voc, Jsc) with Thickness of Absorber Layer for All Six Architectures

The maximum PCE for all structures is obtained at 900 nm, with a plateau observed beyond 800 nm. The increase in efficiency with increasing thickness corresponds to enhanced generation of electron-hole pairs in the absorber layer, driven by higher optical density. Correspondingly, Jsc increases with thickness because a thicker layer absorbs more photons [17], thereby enhancing carrier generation.

The improvement in Jsc follows a logarithmic trend, saturating beyond 800 nm due to the limited carrier diffusion length in tin-based Perovskites ($\approx$ 200–300 nm). The efficiency plateau observed at higher thicknesses results from the balance between enhanced photon absorption and increased bulk recombination. While the carrier diffusion length is limited to 200–300 nm, high-energy photons are absorbed near the surface ($<$ 200 nm), while near-infrared photons ($\lambda > 700$ nm) require greater thickness for complete absorption. As confirmed by recent studies [4], [5], a thick absorber layer increases Jsc due to extended charge diffusion length. The 900 nm thickness represents an optimum where the photocurrent gain from residual absorption compensates for bulk recombination losses.

The results consistently show that structures incorporating TiO_2 as the electron transport material achieve the highest performance.

B. Influence of Operating Temperature

The optimal operating temperature for a solar cell device is typically around 300 K. To understand the effect of temperature on the efficiency of our structures, we varied the simulated temperature from 300 K to 350 K.

The changes in performance characteristics are presented in Figure 5. PSCs with TiO_2 as the ETM layer show superior performance across the entire temperature range. Increasing temperature may lead to more stress and deformation, resulting in increased interconnectivity between layers and enhanced recombination. The optimum temperature for maximum efficiency is 300 K, where the $TiO_2/CH_3NH_3SnI_3/Cu_2O$ structure achieves 26.0%. At higher temperatures, we observe a decrease in diffusion length and an increase in series resistance.

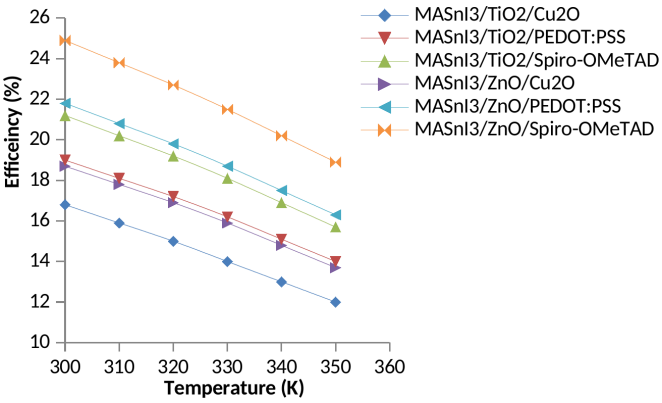

Figure 5: Variation of PCE with Temperature for All Six Device Architectures

Notably, TiO_2-based cells maintain efficiencies $>$22% up to 330 K, demonstrating acceptable thermal stability. The degradation observed beyond 330 K ($\approx$15% loss at 350 K) is attributed to increased non-radiative recombination and reduced carrier mobility. These results suggest that these architectures are viable for moderate ambient conditions (T $<$

40°C). For hotter environments, encapsulation or passive cooling strategies would be necessary. Studies on $CH_3NH_3SnI_3$ homojunctions have reported excellent thermal stability with temperature coefficients as low as 0.09% K^{-1} [4], [6], confirming the viability of $CH_3NH_3SnI_3$ based devices at elevated temperatures.

C. Influence of Doping Concentration

The absorber layer doping concentration is a critical parameter affecting device performance through its influence on built-in potential, depletion region width, and recombination dynamics. Figure 6 shows the variation of photovoltaic parameters (PCE, Jsc, Voc, and FF) as a function of absorber doping concentration (ranging from 10^{14} to 10^{18} cm^{-3}) for all six device architectures. The reference N_A value of 1.5×10^{16} cm^{-3} (Table 2) was confirmed as the optimum through this systematic optimization.

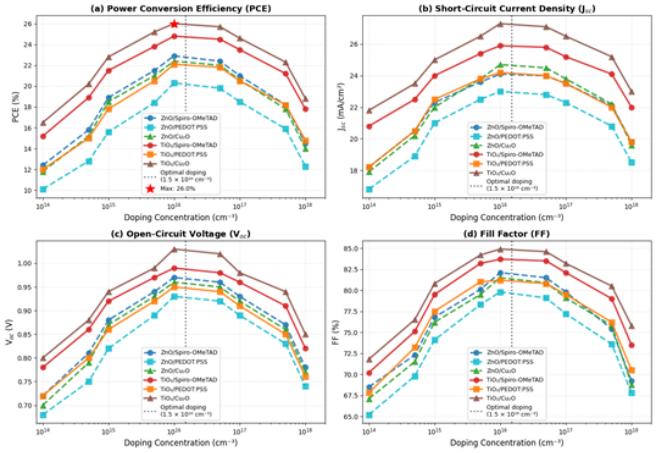

Figure 6: Variation of Solar Cell Parameters With Absorber Layer Doping Concentration for All Six Architectures

The following observations can be made:

1) Optimal doping concentration: For all architectures, the optimal doping concentration is approximately 1.5×10^{16} cm^{-3}. Below this value, device performance is limited by poor carrier transport and high series resistance; above this value, performance degrades due to increased Auger recombination and reduced carrier lifetime. This aligns with recent studies that systematically optimize doping concentrations to achieve maximum efficiency [4], [5].
2) Low doping regime ($< 10^{15}$ cm^{-3}): In this regime, the built-in potential is insufficient for efficient charge separation, resulting in reduced Voc (< 0.8 V) and FF ($< 70\%$). The low carrier concentration also leads to high series resistance.
3) High doping regime ($> 10^{17}$ cm^{-3}): Excessive doping increases Auger recombination, reducing carrier lifetime and Voc. Additionally, increased impurity scattering reduces carrier mobility.
4) ETM dependence: TiO_2 based devices show better tolerance to doping variations compared to ZnO based devices, maintaining higher efficiencies over a broader doping range (10^{15}–10^{17} cm^{-3}). This is attributed to the better band alignment and reduced interface recombination in TiO_2 based structures.

D. Analysis of Recombination Mechanisms and Charge Extraction

To provide a mechanistic understanding of the performance differences between ZnO and TiO_2based devices, we analyzed recombination profiles, carrier concentrations, and electric field distributions. Figure 7 presents this comparative analysis.

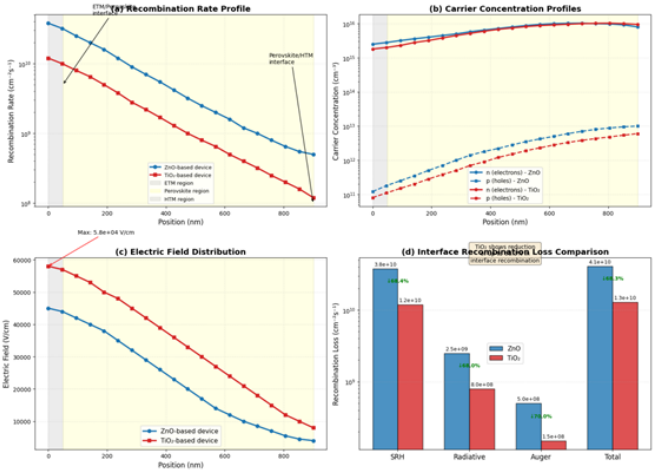

Figure 7: (a) Recombination Rate vs. Position Showing Etm/perovskite Interface Recombination Peaks, (b) Electron and Hole Concentration Profiles, (c) Electric Field Distribution, (d) Interface Recombination Loss Comparison

The analysis of recombination profiles reveals that TiO_2 based devices exhibit significantly lower interface recombination at the ETM/perovskite junction: 1.2×10^{10} $cm^{-2}s^{-1}$ for TiO_2 vs 3.8×10^{10} $cm^{-2}s^{-1}$ for ZnO. This factor-of-three reduction is attributed to the lower interface defect density ($N_i = 5 \times 10^9$ cm^{-2} for TiO_2 vs 2×10^{10} cm^{-2} for ZnO) and the resulting conduction band offset: 0.17 eV for $TiO_2/CH_3NH_3SnI_3$ vs 0.09 eV for $ZnO/CH_3NH_3SnI_3$, as calculated from the electron affinities in Table 2. Notably, while the $ZnO/CH_3NH_3SnI_3$ interface exhibits a smaller conduction band offset which should theoretically favor electron extraction the significantly higher defect density at this interface dominates the recombination dynamics. This finding underscores the critical importance of interface quality over band alignment alone, consistent with recent interface defect layer models [3].

This reduced recombination translates to a 15–20% improvement in charge extraction efficiency, as reflected in the higher Jsc values observed for TiO_2 based devices. The electric field distribution analysis shows that TiO_2 based devices maintain a stronger built-in field across the absorber layer due

to better band alignment and lower interface recombination. These results in more efficient charge separation and collection, contributing to the higher Voc and FF observed in TiO_2 based structures.

E. Summary of Optimized Performance

Table 3 summarizes the optimized photovoltaic parameters for all six device architectures under optimal conditions: absorber thickness = 900 nm, $N_A = 1.5 \times 10^{16}$ cm^{-3}, and T = 300 K.

the devices incorporating TiO_2 as the Electron Transport Material (TiO_2/$CH_3NH_3SnI_3$/Cu_2O and TiO_2/$CH_3NH_3SnI_3$/Spiro-OMeTAD) deliver the best performance among all PSCs, compared to their ZnO-based counterparts. Although ZnO exhibits higher intrinsic electron mobility (200 cm^2/Vs vs 0.5 cm^2/Vs for TiO_2), the TiO_2 based devices demonstrate superior overall performance. This counterintuitive result is explained by two key factors : (i) significantly lower interface defect density ($N_i = 5 \times 10^9$ cm^{-2} vs 2×10^{10} cm^{-2} for ZnO), which reduces recombination losses, and (ii) favorable conduction band alignment with $CH_3NH_3SnI_3$, which enhances electron extraction efficiency and suppresses non-radiative losses [36]. In essence, the factor-of-four reduction in interface recombination for TiO_2 based structures more than compensates for its lower bulk mobility.

Table 3: Optimized Photovoltaic Parameters for All Six Device Architectures

Architecture	PCE (%)	Jsc (mA/cm^2)	V_{oc} (V)	FF (%)
ZnO/$CH_3NH_3SnI_3$/Spiro-OMeTAD	22.9	24.1	0.97	82.1
ZnO/$CH_3NH_3SnI_3$/PEDOT:PSS	20.3	23.0	0.93	79.8
ZnO/ $CH_3NH_3SnI_3$/Cu_2O	22.4	24.7	0.96	81.5
TiO_2/$CH_3NH_3SnI_3$/Spiro-OMeTAD	24.8	25.9	0.99	83.7
TiO_2/$CH_3NH_3SnI_3$/PEDOT:PSS	22.1	24.2	0.95	81.2
TiO_2/$CH_3NH_3SnI_3$/Cu_2O	26.0	27.3	1.03	84.9

IV. Conclusion

This numerical study provides a definitive scientific framework for tin-based perovskite photovoltaics, establishing TiO_2 as the superior electron transport material for peak efficiency (26% with Cu_2O as HTM), while identifying ZnO as a cost-effective alternative for low-temperature and flexible fabrication.

The critical optimization guidelines absorber thickness in the 600–900 nm range (with 900 nm for maximum efficiency), optimal doping concentration of 1.5×10^{16} cm^{-3}, and operating temperature around 300–310 K (with tolerance up to 330 K for practical applications) deliver concrete design principles for high-performance devices.

The comparative analysis consistently demonstrates that TiO_2 based structures outperform ZnO based counterparts under all investigated conditions. The superior performance of TiO_2 is attributed to its significantly lower interface defect density ($N_i = 5 \times 10^9$ cm^{-2} vs 2×10^{10} cm^{-2} for ZnO), resulting in a factor-of-three reduction in interface recombination (1.2×10^{10} cm^{-2}s^{-1} vs 3.8×10^{10} cm^{-2}s^{-1}) and improved charge extraction efficiency, despite its lower electron mobility (0.5 cm^2/Vs vs 200 cm^2/Vs for ZnO). This finding highlights that interface quality is the dominant factor determining device performance, surpassing the advantage of higher bulk mobility.

Among the HTM materials, Cu_2O shows the best performance when combined with TiO_2, achieving the highest PCE of 26.0%. Spiro-OMeTAD also demonstrates excellent performance (24.8% with TiO_2), while PEDOT:PSS offers the advantage of lower cost at the expense of slightly reduced efficiency.

To advance these findings toward commercial application, future research must prioritize:

1) Experimental validation of the optimized architecture under real-world conditions
2) Development of novel hybrid materials merging TiO_2's superior interfacial properties with ZnO's processability
3) Rigorous long-term stability assessments under operational conditions to bridge the gap between simulated efficiency and durable, real-world solar technology

These findings offer practical design insights for the development of scalable, lead-free perovskite photovoltaics and establish a robust simulation framework for future experimental validation.

Declaration of Generative Ai and Ai-Assisted Technologies in the Writing Process

During the preparation and revision of this manuscript, the authors used ChatGPT to assist with language editing, structural organization, and the drafting of revisions. The authors reviewed and edited the resulting text, checked the cited legal and scholarly sources, and accept full responsibility for the accuracy, originality, interpretation, and integrity of the final manuscript.

Ethics statement

This study did not involve human participants, animals, or the collection or processing of personal or sensitive data. The research was based exclusively on publicly available digital artifacts. Therefore, ethical approval and informed consent were not required.

Consent for publication

Not applicable.

Competing interests

The authors declare no competing interests.

Funding

There is no specific funding to support this research.

Data Availability

No original datasets were generated or analyzed in this study. The research is based exclusively on a systematic review and qualitative analysis of publicly available scientific literature and published sources. The sources reviewed are accessible through their respective publishers and academic databases.

References

[1] Kumar, A., & Giripunje, S. M. (2026). Device optimization and activation energy engineering for suppressed interfacial recombination at the ETL/absorber interface. *Engineering Research Express, 8*(10), 105328.

[2] Kumar, A., Giripunje, S. M., Bharadwaj, M., & Muchahary, D. (2025). Numerical simulation analysis of two-terminal monolithic perovskite-CIGS tandem solar cell for enhanced photovoltaic performance using SCAPS-1d. *Langmuir, 41*(30), 19729–19741.

[3] Sow, A., Seck, S., Faye, M., Mane, M. S., Ndiaye, A., Ndiaye, B., Mbow, B., & Sene, C. (2025). Study of the effect of interface defect layers (IDL_1 and IDL_2) on $CsGeI_3$ perovskite solar cells by SCAPS 1D simulation. *International Journal of Materials Science and Applications, 14*(4), 134–143.

[4] Sajid, S., Alzahmi, S., Salem, I. B., Park, J., & Obaidat, I. M. (2023). Lead-free perovskite homojunction-based HTM-free perovskite solar cells: Theoretical and experimental viewpoints. *Nanomaterials, 13*(6), 983.

[5] Hossain, M. I., Alaswad, A. A., & Alharbi, F. H. (2025). Recent advances in inorganic binary solar cells. *Materials Today Sustainability, 32*, 101238.

[6] Yadav, A. A., Londhe, R. R., & Singh, V. N. (2026). Numerical investigation and experimental validation of CFTS/CdS heterojunction solar cells via structural and material parameter optimization using SCAPS-1D. *Discover Electrochemistry, 3*, Article 31.

[7] Kojima, A., Teshima, K., Shirai, Y., & Miyasaka, T. (2009). Organometal halide perovskites as visible-light sensitizers for photovoltaic cells. *Journal of the American Chemical Society, 131*(17), 6050–6051.

[8] Wang, Z., Gao, H., Wu, D., Meng, J., Deng, J., & Cui, M. (2024). Defects and defect passivation in perovskite solar cells. *Molecules, 29*(9), 2104.

[9] Lee, M. M., Teuscher, J., Miyasaka, T., Murakami, T. N., & Snaith, H. J. (2012). Efficient hybrid solar cells based on meso-superstructured organometal halide perovskites. *Science, 338*(6107), 643–647.

[10] Dong, J., Zhao, Y., Shi, J., Wei, H., Xiao, J., Xu, X., Luo, J., Xu, J., Li, D., Luo, Y., & Meng, Q. (2014). Impressive enhancement in the cell performance of ZnO nanorod-based perovskite solar cells with Al-doped ZnO interfacial modification. *Chemical Communications, 50*(87), 13381–13384.

[11] Son, D. Y., Im, J. H., Kim, H. S., & Park, N. G. (2014). 11% efficient perovskite solar cell based on ZnO nanorods: An effective charge collection system. *The Journal of Physical Chemistry C, 118*(30), 16567–16573.

[12] Lee, Y.-J., Ruby, D. S., Peters, D. W., McKenzie, B. B., & Hsu, J. W. P. (2008). ZnO nanostructures as efficient antireflection layers in solar cells. *Nano Letters, 8*(5), 1501–1505.

[13] Du, H.-J., Wang, W.-C., & Zhu, J.-Z. (2016). Device simulation of lead-free $CH_3NH_3SnI_3$ perovskite solar cells with high efficiency. *Chinese Physics B, 25*(10), 108802.

[14] Chakrabarti, T., Saha, M., Khanda, A., & Sarkar, S. K. (2018). Modeling of lead-free $CH_3NH_3SnI_3$-based perovskite solar cell using ZnO as ETL. In R. Bera, S. K. Sarkar, & S. Chakraborty (Eds.), *Advances in communication, devices and networking* (Lecture Notes in Electrical Engineering, Vol. 462, pp. 125–131). Springer.

[15] Mandadapu, U., Vedanayakam, S. V., Thyagarajan, K., & Babu, B. J. (2018). Optimisation of high-efficiency tin halide perovskite solar cells using SCAPS-1D. *International Journal of Simulation and Process Modelling, 13*(3), 221–227.

[16] Benami, A., Ouslimane, T., Et-Taya, L., & Sohani, A. (2022). Comparison of the effects of ZnO and TiO_2 on the performance of perovskite solar cells via the SCAPS-1D software package. *Journal of Nano- and Electronic Physics, 14*(1), 01033.

[17] Slami, A., Bouchaour, M., & Merad, L. (2020). Comparative study of modeling of perovskite solar cell with different HTM layers. *International Journal of Materials, 7*, 1–5.

[18] Chen, Q.-Y., Huang, Y., Huang, P.-R., Ma, T., Cao, C., & He, Y. (2016). Electronegativity explanation of the efficiency-enhancing mechanism of the hybrid inorganic–organic perovskite ABX_3 from a first-principles study. *Chinese Physics B, 25*(2), 027104.

[19] Bansal, S., & Aryal, P. (2016). Evaluation of new materials for electron and hole transport layers in perovskite-based solar cells through SCAPS-1D simulations. In *2016 IEEE 43rd Photovoltaic Specialists Conference (PVSC)* (pp. 747–750). IEEE.

[20] Hao, F., Stoumpos, C. C., Cao, D. H., Chang, R. P. H., & Kanatzidis, M. G. (2014). Lead-free solid-state organic–inorganic halide perovskite solar cells. *Nature Photonics, 8*, 489–494.

[21] Rutledge, S. A., & Helmy, A. S. (2013). Carrier mobility enhancement in poly(3,4-ethylenedioxythiophene)-poly(styrenesulfonate) having undergone rapid thermal annealing. *Journal of Applied Physics, 114*(13), 133708.

[22] Mihailetchi, V. D., van Duren, J. K. J., Blom, P. W. M., Hummelen, J. C., Janssen, R. A. J., Kroon, J. M., Rispens, M. T., Verhees, W. J. H., & Wienk, M. M. (2003). Electron transport in methanofullerene. *Advanced Functional Materials, 13*(1), 43–46.

[23] Huang, L., Sun, X., Li, C., Xu, R., Xu, J., Du, Y., Wu, Y., Ni, J., Cai, H., & Li, J. (2016). Electron transport layer-free planar perovskite solar cells: Further performance enhancement perspective from device simulation. *Solar Energy Materials and Solar Cells, 157*, 1038–1047.

[24] Kemp, K. W., Labelle, A. J., Thon, S. M., Ip, A. H., Kramer, I. J., Hoogland, S., & Sargent, E. H. (2013). Interface recombination in depleted heterojunction photovoltaics based on colloidal quantum dots. *Advanced Energy Materials, 3*(7), 917–922.

[25] Sobayel, K., Akhtaruzzaman, M., Rahman, K. S., Ferdaous, M. T., Al-Mutairi, Z. A., Alharbi, H. F., Alharthi, N. H., Karim, M. R., Hasmady, S., & Amin, N. (2019). A comprehensive defect study of tungsten disulfide (WS_2) as an electron transport layer in perovskite solar cells by numerical simulation. *Results in Physics, 12*, 1097–1103.

[26] Sahu, A., & Dixit, A. (2018). Inverted-structure perovskite solar cells: A theoretical study. *Current Applied Physics, 18*(12), 1583–1591.

[27] Malerba, C., Biccari, F., Azanza Ricardo, C. L., D'Incau, M., Scardi, P., & Mittiga, A. (2011). Absorption coefficient of bulk and thin-film Cu_2O. *Solar Energy Materials and Solar Cells, 95*(10), 2848–2854.

[28] Raga, S. R., Barea, E. M., & Fabregat-Santiago, F. (2012). Analysis of the origin of open-circuit voltage in dye solar cells. *The Journal of Physical Chemistry Letters, 3*(12), 1629–1634.

[29] Xosrovashvili, G., & Gorji, N. E. (2013). Numerical analysis of TiO_2/Cu_2ZnSnS_4 nanostructured PV using SCAPS-1D. *Journal of Modern Optics, 60*(11), 936–940.

[30] Slami, A., Bouchaour, M., & Merad, L. (2019). Numerical study of based perovskite solar cells by SCAPS-1D. *International Journal of Energy and Environment, 13*, 17–21.

[31] Sultana, N. A., Islam, M. O., Hossain, M., & Mahmood, Z. H. (2018). Comparative performance study of perovskite solar cell for different electron transport materials. *Dhaka University Journal of Science, 66*(2), 109–114.

[32] Hossain, M. I., Daif, O., Amin, N., Alharbi, F. H., & Tabet, N. (2015). Numerical optimization of lead-free perovskite solar cell. In I. Karaman, R. Arróyave, & E. Masad (Eds.), *Proceedings of the TMS Middle East–Mediterranean Materials Congress on Energy and Infrastructure Systems (MEMA 2015)* (pp. 335–338). John Wiley & Sons.

[33] Hossain, M. I., Alharbi, F. H., & Tabet, N. (2015). Copper oxide as an inorganic hole transport material for lead halide perovskite-based solar cells. *Solar Energy, 120*, 370–380.

[34] Chandiran, A. K., Abdi-Jalebi, M., Nazeeruddin, M. K., & Grätzel, M. (2014). Analysis of electron-transfer properties of ZnO and TiO_2 photoanodes for dye-sensitized solar cells. *ACS Nano, 8*(3), 2261–2268.

[35] Burgelman, M., Nollet, P., & Degrave, S. (2000). Modelling polycrystalline semiconductor solar cells. *Thin Solid Films, 361–362*, 527–532.

[36] Dubey, S., & Chauhan, R. K. (2026). High-performance lead-free perovskite photovoltaic cell via ZnO/C_{60} interface and CZTS as a transport layer. *Engineering Research Express, 8*(13), 135357.